Reverse-Taper Mid-Infrared Quantum Cascade Lasers for Coherent Power Scaling

Jae Ha Ryu, Benjamin Knipfer, Jeremy D. Kirch, *Member, IEEE*, Robert A. Marsland, *Senior Member, IEEE*, Dan Botez, *Life Fellow, IEEE*, Tom Earles, Chris Galstad, Morgan Turville-Heitz, Chris Sigler, *Member, IEEE*, Axel Strömberg, Yan-Ting Sun, Sebastian Lourdudoss, *Senior Member, IEEE*, and Luke J. Mawst, *Fellow, IEEE*

***Abstract*—We present a reverse-taper quantum cascade laser (QCL) emitting at 4.6 μm, a novel-geometry device that can scale the output power while maintaining good beam quality. Buried-ridge waveguides with tapered and straight regions were formed by ICP etching and HVPE regrowth – the tapered region scales the output power, while the emitting facet is located at the narrow-end taper section, which provides mode filtering by suppressing high-order spatial modes. Beam profiles were observed under quasi-continuous-wave (QCW)/CW operation and beam quality (M^2) measurements along with beam-stability measurements were performed – a small degree of collimated-beam centroid movement ($<$0.46 mrad, peak-to-peak) was observed, along with M^2 values close to 1 up to $\sim$1 W QCW power. Devices of shorter cavity lengths were also investigated, indicating that the output power scales with the core-region volume but results in a small increase in angular deviation.**

***Index Terms*—Quantum cascade lasers, beam steering, semiconductor growth.**

I. Introduction

SEMICONDUCTOR quantum cascade lasers (QCLs) emitting in the mid-infrared (IR) range (i.e., 3-10 μm) are currently of great interest for various applications such as remote spectroscopic sensing of toxic-chemical agents, infrared countermeasures, free-space communications, and LIDAR. High brightness (i.e., high power with good beam quality) is desired for many of these applications. However, increasing the brightness of QCLs remains a challenge. QCLs, in general, are limited in maximum continuous-wave (CW) power due to device shutoff or thermal rollover. First, field-induced shutoff occurs when increasing the applied electric field causes the injecting state to rise above the upper laser level, thus carrier injection ceases and shuts off the laser. Second, thermal rollover occurs when the CW power saturates due to changes in threshold and slope efficiency with increasing temperature, as the device core region is subject to self-heating. Thus, the maximum CW power that can be obtained from a QCL is constrained by both the size of the core-region volume and by the degree of heat removal [1]. The core-region volume is the product of the core-region thickness (i.e., the number of stages $\times$ stage thickness) and the pumped-region area (i.e., the length of cavity $\times$ width of the core region). Simply increasing the volume of the core region has limitations – increasing the number of stages increases the operating voltage and core-region temperature; increasing the length is limited by internal loss as it significantly reduces the slope efficiency; and increasing the emitter width decreases the heat-removal effectiveness in quasi-CW (QCW)/CW operation [1] and leads to multi-spatial-mode operation.

Many approaches have been investigated for achieving high-power ($>$1 W) single-mode CW output powers, among them are the use of monolithic phase-locked laser array structures and multimode-interferometer (MMI)-combined tree-array structures. Leaky-wave-coupled phase-locked antiguided-laser arrays [2]–[8] have successfully achieved single-spatial-mode operation from large emitting apertures. Such devices possess a large built-in index contrast and operate in an in-phase array mode with uniform intensity profile across the emitting aperture, which ensures mode stability even under CW operation. Similarly, MMI tree-array structures [9] ensure single-spatial-mode operation to high CW powers, but, due to an inherently low fill factor, they emit in heavily multi-lobed (i.e., 35 lobes) beam patterns. Even though phase-locked arrays are a proven solution for scaling the CW power of QCLs, the fabrication processes involved are more complex than those employed for the fabrication of single-element devices.

For single-element devices, longitudinally tapering the laser stripe width, has been an attractive method to achieve increased brightness. This type of device [10] typically has a straight section and a tapered section, and for QCLs it has been implemented either as master-oscillator power amplifiers (MOPAs) [11]–[13], or as tapered lasers, where for both device types the emitting facet is on the flared, wide end of the facet. The MOPA uses the

Manuscript received February 4, 2022; revised March 23, 2022; accepted March 27, 2022. Date of publication March 31, 2022; date of current version April 21, 2022. The work of D. Botez and L. J. Mawst have significant financial interest supported by the University of Wisconsin–Madison by Intraband, LLC. The work at KTH was supported in part by Swedish Research Council under Grant 2015-05470 and in part by EU HORIZON 2020 under Grant 828893. This work was supported in part by the AFOSR under Grant FA9550-19-1-0385 and in part by the ARO under Grant W911-NF-16-C-0116. *(Corresponding author: Luke J. Mawst.)*

Jae Ha Ryu, Benjamin Knipfer, Jeremy D. Kirch, Dan Botez, Morgan Turville-Heitz, Chris Sigler, and Luke J. Mawst are with the University of Wisconsin–Madison, Madison, WI 53706 USA (e-mail: jryu34@wisc.edu; bknipfer@wisc.edu; jdkirch@wisc.edu; botez@engr.wisc.edu; mturville-hei@wisc.edu; casigler@wisc.edu; mawst@engr.wisc.edu).

Robert A. Marsland is with the Intraband, LLC, Madison, WI 53726 USA (e-mail: rmarsland@intraband.net).

Tom Earles and Chris Galstad are with the DRS Daylight Solutions, Madison, WI 53704 USA (e-mail: tom.earles@drs.com; chris.galstad@drs.com).

Axel Strömberg, Yan-Ting Sun, and Sebastian Lourdudoss are with the KTH Royal Institute of Technology, 114 28 Stockholm, Sweden (e-mail: axestr@kth.se; yasun@kth.se; slo@kth.se).

Digital Object Identifier 10.1109/JPHOT.2022.3163409

narrow section as the master oscillator, and the tapered region as the gain region that acts as a power amplifier. The MOPAs, however, are extremely sensitive to back reflections (a very low reflectivity coating on the emitting facet is required) and have no lateral built-in index structure which makes them susceptible to any perturbations in index, especially due to thermal lensing in CW operation [10].

Tapered lasers have very similar geometries as MOPAs, but both the straight and tapered region form the laser cavity. In the case of diode lasers, tapered lasers can be an attractive method – large emitting aperture reduces the optical-power density at the facet and suppresses failures due to catastrophic optical mirror damage (COMD) and allows for higher reliable output powers. This tapered laser approach has also been implemented for QCLs. A tapered QCL with emitting wavelength $\lambda \sim 4.6\ \mu$m with 4.5 W CW output power was demonstrated [14] – even though the beam had a single-lobe pattern, the device operated multimode, as evidenced from a broad beam pattern. Another tapered QCL was demonstrated, at $\lambda \sim 8.1\ \mu$m, with 4.3 W peak pulsed output power and beam quality factor of $M^2 \sim 1.6$ [15].

For tapered QCLs, where the emitting aperture is on the wide, flared-end, taking this approach may be limited because the self-heating effects are much stronger for QCLs. CW operation can cause multimode operation and/or beam steering from gain spatial-hole burning and/or thermal lensing. Surface recombination and/or optical absorption at the laser facet are not issues because QCLs are unipolar intersubband-transition devices. While QCLs can still fail by thermal shear stress at the laser facet [16], unlike near-IR, interband-transition lasers, light is not absorbed at the facets. Thus, high optical-power densities do not contribute to failures at the wavelength we are considering; that is, $\sim 4.6\ \mu$m. As a result, widening the emitting aperture to reduce the optical-power density is not necessary for QCLs. However, widening of the buried-ridge width internally or at the non-emitting facet (i.e., the HR-coated facet) will allow for scaling the core-region volume, and subsequently increasing the maximum output power. Here we propose and demonstrate a novel-geometry device: reverse-taper QCL, where the emitting facet is located at the narrow taper end, in order to scale the core-region volume and provide a spatial-mode filter for suppressing lasing in high-order spatial modes. Reverse-taper QCLs of different taper widths and cavity lengths were investigated, and the result is that the output power can be scaled without significant compromise in beam quality, with M^2 values <1.5 and beam-centroid deviation of <0.5 mrad for all devices studied.

II. Experiments

A 35-stage, 4.6 μm-emitting MOCVD-grown, step-tapered active-region (STA) structure [17] was used. A deep ridge was formed by using ICP etching, followed by a brief wet etch to clean the ICP-induced damage. The reverse-taper structure was formed with varying ridge width along the longitudinal direction, as shown in the schematic top view of the device (Fig. 1). The device has a total length of 7 mm, where the length of the straight narrow section ($L_{straight}$) is 1 mm, and the length of the tapered region (L_{taper}) is 6 mm. A parabolic

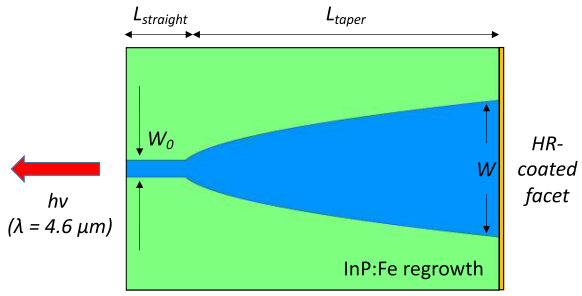

Fig. 1. Schematic of the reverse-taper QCL structure.

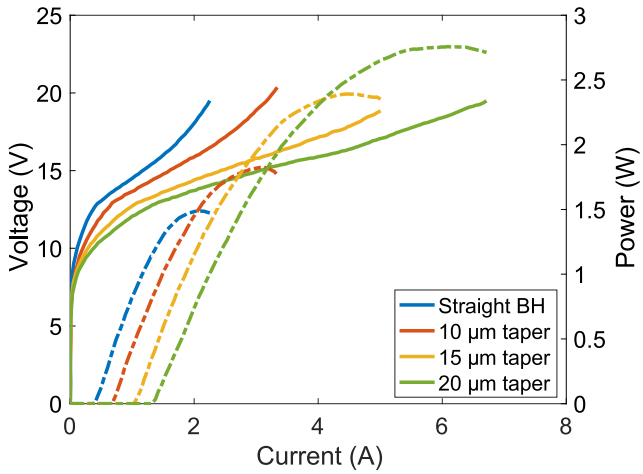

Fig. 2. Measured L-I (dot-dash curves) and V-I (solid curves) data for representative 7 mm-long reverse-taper and straight BH devices under short-pulse drive conditions (200 ns-wide pulses, 20 kHz rep. rate).

taper [18] was used for all devices – the equation for the wide-end width of the taper is $W = \sqrt{\frac{2\alpha\lambda z}{n_{eff}} + W_0^2}$, where α is a constant <1 and W_0 is the width of the narrow section. Reverse-taper buried-heterostructure (BH) devices of varying wide-end widths ($W = 10, 15, 20\ \mu$m) were fabricated, along with a regular straight BH device as a reference, of $\sim 4.5\ \mu$m-wide buried ridge.

Using an SiO_2 hardmask, selective regrowth of semi-insulating InP was performed using Hydride Vapor Phase Epitaxy (HVPE), similar to that reported previously [19]. While MOCVD is commonly used for selective regrowths, it is known to be dependent on processing conditions such as the regrowth thickness and the lateral undercut depth under the hard mask. HVPE, on the other hand, is much less dependent on such factors, and highly planar top surfaces can be obtained at a high growth rate. After the regrowth, a nitride layer was deposited and patterned for the metal contact window on the top of the buried ridge, and then the metal layer was evaporated, followed by lapping and back-side metallization. The taper-wide-end facet was then HR-coated, while the emitting facet was left uncoated.

All measurements were done with a measurement-stage temperature maintained at 20 °C. The devices were first tested under short-pulse conditions (200 ns-wide pulses, 20 kHz rep. rate). Fig. 2 shows the light-current-voltage (L-I-V) data of representative reverse-taper devices of 10 μm, 15 μm, and 20 μm wide-end taper widths, along with those for a regular

straight BH, for reference. It can be clearly seen that the output powers and thresholds scale with the volume of the core region. In most cases, without heating, we observe little difference between the slope efficiencies of straight and tapered devices, as is evident from Fig. 2. The slope efficiencies are 1.31, 1.27, 1.32, 1.12 W/A, for the straight BH, and the 10 μm, 15 μm, 20 μm taper devices, respectively. However, in some cases the pulsed slope- efficiency values of tapered devices can actually be higher than than those of straight devices. This may reflect that fact that there are absorption losses to the metal on both sides of $\sim$4.5 μm-wide buried ridges [19] and the degree of absorption may vary among devices, leading to higher internal losses and correspondingly lower slope efficiency.

The beam quality of these devices was also evaluated – the beam quality factor, more commonly known as M^2, was calculated by the method described in the ISO standard [20]. The measurement setup for the M^2 calculation consists of a $\sim$1.8 mm focal length high-NA collimating lens, a focusing mirror (focal length $\sim$500 mm), and a camera that consists of 160 $\times$ 160 pixels. The camera is moved along the beam path and 10 images of the focused-beam profile are taken to measure how the beam focuses and diverges. The beam waist is measured and using the data a curve fit is performed to express the beam waist along the propagation distance: $d_\sigma(z) = \sqrt{a + bz + cz^2}$, where *a*, *b*, and *c* are the fit parameters, and *z* is the distance along the beam path. From the fit parameters, the M^2 value can be calculated as such: $M^2 = \frac{\pi}{8\lambda}\sqrt{4ac - b^2}$, along with the divergence angle: $\theta = \sqrt{c}$, along both x and y directions.

The beam stability of the devices was also investigated using a slightly different setup – instead of the 500 mm focal length mirror, a focusing mirror with 2032 mm focal length is placed approximately 1 m after the collimating lens, and the camera is placed at the focal plane of the focusing mirror. The far-field beam profile images can be taken, and the beam stability is evaluated by the far-field beam centroid movement. The far-field beam centroid position is measured at different drive currents, and the angular deviation can then be found by first subtracting the mean centroid location (in microns) to get the deviation and then dividing by the focal length of the focusing mirror (2032 mm) to convert into an angle in milliradians. This method of evaluating the beam stability, compared to the typical method of evaluating the peak position change of the beam directly coming out of the laser, is a more sensitive measure of beam deviation and is also more meaningful in an application perspective.

III. Results

A set of devices consisting of a straight BH and 10 μm- and 20 μm-wide reverse-taper wide ends were mounted epi-side down using indium solder to measure their QCW/CW characteristics. A representative SEM cross-section image of the emitting facet (narrow section) of a reverse-taper device is shown in Fig. 3 – the vertical sidewalls from ICP etching and a well-planarized top surface, on both sides of the buried ridge, as a result of HVPE regrowth can be seen.

L-I-V characteristics and 2-D collimated beam profiles were measured using a $\sim$1.8 mm focal length collimating lens.

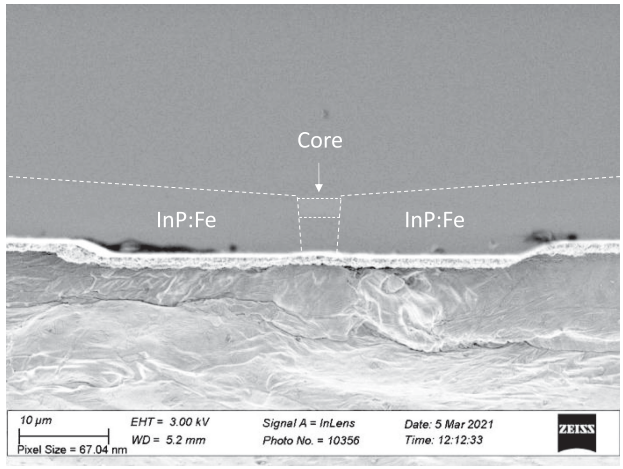

Fig. 3. SEM cross section of the emitting facet (narrow section) of a representative reverse-taper device.

Fig. 4(a) below shows the L-I-V curves and the 2-D beam profiles of these devices under short-pulse drive conditions (200 ns pulse-width, 20 kHz rep. rate). From the 2-D beam profiles one can see that for the straight-BH and the 10 μm reverse-taper devices, the beam is stable up to rollover, whereas for the 20 μm-wide reverse-taper device the beam starts to broaden at high currents. These devices were then measured under QCW conditions (100 µs pulse width) as shown in Fig. 4(b) – the beam profiles are similar to those in the short-pulse case, but we noticed more beam broadening for the 20 μm-wide taper device at high currents (i.e., near the rollover current).

The beam-quality factors (M^2) of the devices were then measured under QCW (100 µs pulse width) conditions, followed by beam-stability measurements, as described in the previous section. Unfortunately, the 10 μm-wide tapered device failed during the M^2 measurement – we believe that was due to poor indium bonding. The measured M^2 values and beam stability (angular deviation of the centroid position) as a function of drive current, for the straight BH and the 20 μm-wide taper device, are shown in Fig. 5 below – the red curves correspond to M^2, and the blue curves correspond to angular displacement. The M^2 values along the y-direction is close to 1 for both devices, which is expected as high-order modes are cut-off in the transverse direction due to the narrow aperture ($\sim$2 μm-thick core region). Along the x-direction, the increasing M^2 values from the 20 μm-wide-taper device at currents $>$2 A indicate that the device is operating multimode, although it maintains an M^2 value less than 1.5 up to $\sim$1.4 W QCW output power (i.e., before rollover at $\sim$ 3.2 A). Similar to the M^2 values, the beam stability along the transverse direction (y) exhibits negligible angular deviations. The angular deviation along the lateral (x) direction does fluctuate compared to the transverse (y) direction, but it is within $<$0.46 mrad (peak-to-peak) for all devices, which corresponds to a $\sim$ 4.6 cm targeting error over a 100 m distance. While we were not able to collect M^2 data for the 10 μm-wide taper device, we were able to measure its beam stability, which had an angular deviation $<$0.43 mrad (not shown), that is, similar to the value for the 20 μm-wide taper device.

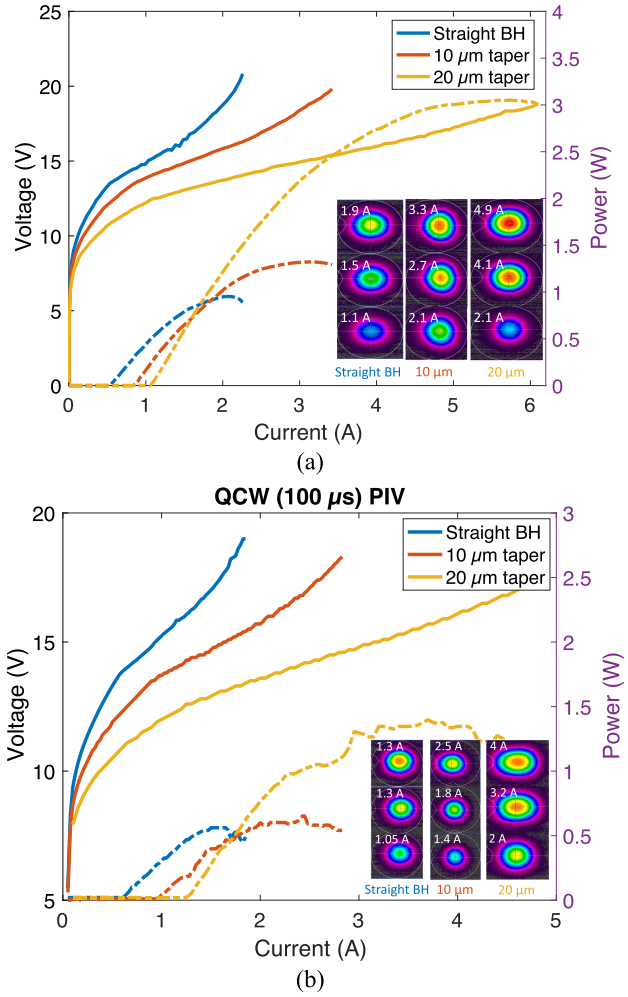

Fig. 4. Measured L-I-V data and the corresponding far-field beam profiles at different operating currents for the 7 mm-long straight BH, 10 μm reverse-taper, and 20 μm reverse-taper devices under (a) short-pulse drive conditions (200 ns-wide pulses), and (b) QCW drive conditions (100 µs-wide pulses).

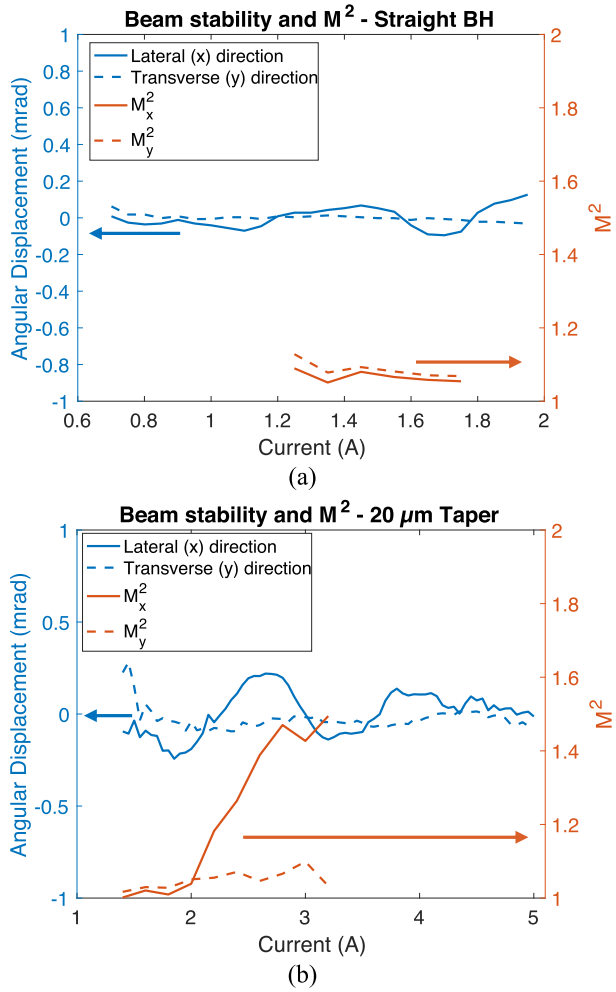

Fig. 5. Measured beam quality factor (M^2) and angular deviation of the collimated-beam far-field centroid position along the x- (lateral) and y- (transverse) directions, as a function of current for the 7 mm-long (a) straight BH, and (b) 20 μm-wide reverse-taper BH under QCW drive conditions.

These devices were also measured under CW operation and were driven up to the highest possible current values from our current-test setup. The L-I-V data and beam profiles are shown below in Fig. 6. As can be seen from the 2D beam profiles, stable single-lobed beams were observed for both devices. In particular, the 20 μm-wide taper device maintained a stable beam up to 600 mW CW power (the CW output power was limited by the heat-removal capability of the testing stage). That is, stable, single-mode CW operation was obtained to basically the same peak power as in QCW operation [Figs. 4(b) and 5(b)], thus proving that in CW operation the additional device heating did not affect the beam quality, to at least 600 mW. It should be noted that the color scale of the beam profiles has been adjusted as needed at higher powers – it cannot be used to compare the intensity between the different current values as it is showing a relative intensity.

To better understand the effect of the taper wide-end width and cavity length on device performance, additional devices of different lengths were investigated. These devices were cleaved to obtain a shorter cavity length (L = 4.5 mm) from existing

TABLE I
TAPER WIDTHS AT THE BACK FACET VS. CAVITY LENGTH

	Back-facet width for L = 7 mm	Back-facet width for L = 4.5 mm
Straight BH	~ 4.5 µm	~ 4.5 µm
10 µm taper	~ 10 µm	~ 8.3 µm
20 µm taper	~ 20 µm	~ 15.6 µm

7 mm-long devices. The straight 1 mm-long narrow section remains unchanged, and the cleave was positioned on the tapered-end side, so the devices have a tapered-region length of 3.5 mm. Also, the tapers' wide-end widths (i.e., at the HR-coated facet) vary for different cavity lengths (see Table I).

For improved QCW/CW performance, these devices were packaged using AuSn solder on AlN submounts, which has better heat removal capabilities due to its high thermal conductivity compared to indium solder. The AlN submounts were attached onto a copper heatsink using SAC (Tin-silver-copper) solder. Analysis on the effect of the different cavity length/taper widths on the device characteristics were performed. The measured L-I

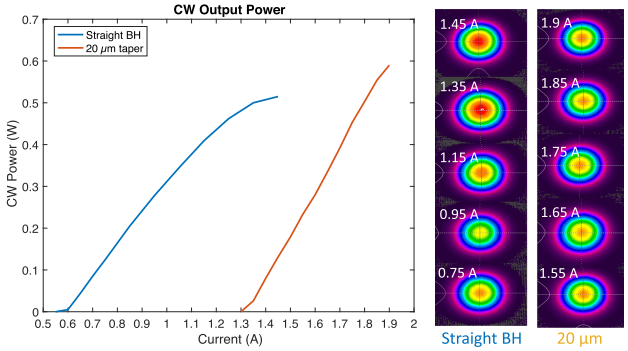

Fig. 6. Measured L-I-V data and far-field beam profiles at different operating currents for the 7 mm-long straight BH and 20 μm-wide reverse-taper devices under CW operating conditions.

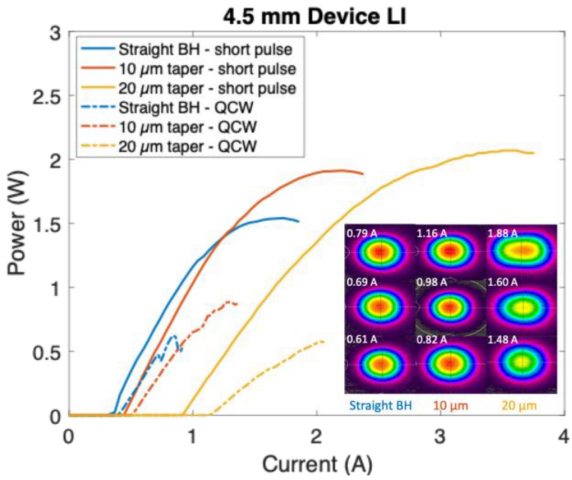

Fig. 7. Measured pulsed (200 ns) and QCW (100 µs) L-I data and beam profiles of shorter cavity length (L = 4.5 mm) devices.

data and beam profiles of devices are shown in Fig. 7 below. From the L-I curves it could be seen that the QCW output power dropped considerably compared to the pulsed output power for all three devices but the power of the 20 μm taper device dropped the most – the output power dropped even lower than the straight BH device. We suspect that this may be due to the poor submount attach for this sample, which prevented efficient heat removal for this device. The beam profile obtained from the 20 μm taper device also shows broadening, as we have seen from the 7 mm-long 20 μm taper device case.

Devices with cavity lengths of L = 4.5 mm and 7 mm are compared, with taper widths of 10 μm and 20 μm (the taper widths for L = 4.5 mm are narrower, as shown in Table I), along with the straight BH as a reference. The devices were evaluated by comparing the beam stability, beam divergence, and the radiant intensity. Fig. 8(a) and (b) are plots of the beam stability and beam divergence (in the x-direction) as a function of maximum QCW power, respectively, and Fig. 8(c) compares the radiant intensity (radiant power emitted per unit solid angle) as a function of the QCW efficiency (ratio of QCW output power to input electrical power). The 7 mm devices are plotted as squares, where the size of the markers reflect the width of the tapers – the

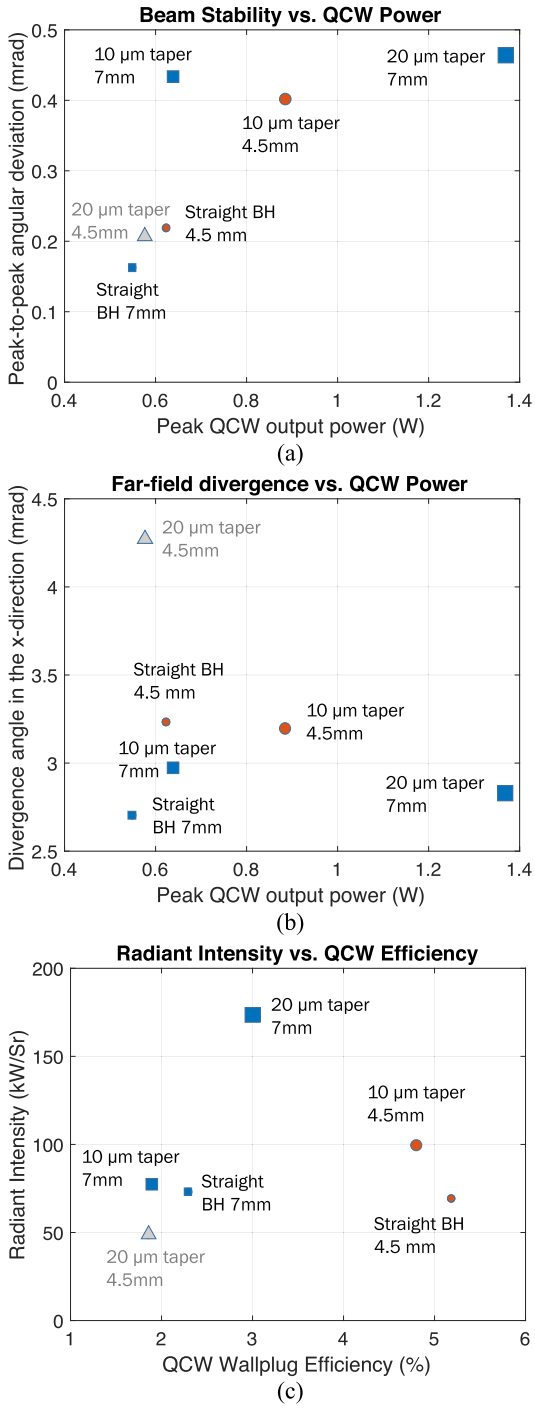

Fig. 8. Plot of (a) peak-to-peak angular deviation and (b) far field divergence angle in the x-direction as a function of QCW peak power, and (c) radiant intensity as a function of QCW wallplug efficiency.

larger the marker, the wider the taper width. It should be noted that the 20 μm taper from the 4.5 mm-long device is shown as a triangle – because of the poor submount attach we believe the data from this device may be an outlier.

From these plots, we can note the following: comparing the tapered devices to the straight BH devices, we can see that scaling the volume by increasing the taper width does decrease the beam stability (i.e., increases the angular deviation) but it comes

at a relatively small cost, as the deviation is still < 0.5 mrad for the tapered devices, compared to 0.2-0.25 mrad for the straight BHs. The output power, on the other hand, can be improved greatly – we can see that the devices with more core-region volume (i.e., the longer devices) had higher output power with the exception of the straight BHs – the 4.5 mm-long straight BH may have better QCW output power compared to the 7 mm-long straight BH due to the improved heat-removal capability. Also, comparing the reverse-taper devices vs. straight BH devices, we can see that the beam divergence can be kept at similar levels while increasing the output power. It should be noted that while the 7 mm-long devices look like they have much lower divergence angle compared to the 4.5 mm-long devices, that it is due to the zoomed-in y-axis scale, while the difference is actually minor. The tapered devices also have improved radiant intensity while having similar wall-plug efficiency values compared to the straight BH devices. As expected, the short-cavity length devices have higher wall-plug efficiency values compared to the long-cavity devices.

In addition to these observations, there are some other things that should be noted from the experiments. The addition of the tapered section made the thermal conductance worse, which is expected, and we were not able to reach higher drive currents as we normally would be able to when using the straight BHs (as shown in Fig. 6), so a more comprehensive study of the beam properties at higher drive currents for the tapered devices could not be done. Also, the beam performance of the taper devices is not very well controlled – at this moment, there does not seem to be a clear relationship between the taper geometry to the beam performance. Additional studies to improve the thermal conductance and better control the mode properties are still needed– optical simulations and additional experimental studies of the impact of the taper geometry (length of the straight section length, taper width, etc.) will be the subject of future studies.

IV. Conclusion

In conclusion, we present a new design for QCLs as a promising approach for increasing the device brightness. While phase-locked laser arrays are still a good option, the presented method has much simpler processing and higher fabrication-error tolerance. Devices of different taper widths were fabricated with a cavity length of 7 mm (1 mm straight, 6 mm tapered), and peak-to-peak centroid motion of less than 0.45 mrad was observed, while an M^2 value of less than 1.5 was measured up to the maximum output power for 20 μm-wide taper devices. The devices were also tested under CW operating conditions, in which case stable, single-lobe beams were observed up to $\sim$600 mW. Additional devices with shorter cavity lengths were mounted using AuSn and AlN submounts – devices of different cavity lengths and taper widths were compared. The beneficial effect that scaling of the core-region volume has on the output power and radiant intensity can clearly be seen, while it comes at a small cost of slightly degraded beam stability. To improve the beam quality under QCW operation, the use of QCL active regions enabling much higher wall-plug efficiencies [17], [21], as well as improved heat management techniques, such as diamond heat spreaders are needed. Additional optical simulation studies and experimental work are also being done to further optimize the device geometry.

References

[1] D. Botez, C.-C. Chang, and L. J. Mawst, "Temperature sensitivity of the electro-optical characteristics for mid-infrared (λ = 3-16 μm)-emitting quantum cascade lasers," *J. Phys. D: Appl. Phys.*, vol. 49, no. 4, 2016, Art. no. 043001.

[2] H. Yang, L. J. Mawst, and D. Botez, "1.6 W continuous-wave coherent power from large-index-step (Δn $\cong$ 0.1) near-resonant, antiguided diode laser arrays," *Appl. Phys. Lett.*, vol. 76, no. 10, pp. 1219–1221, 2000.

[3] D. Botez, L. J. Mawst, and G. Peterson, "Resonant leaky-wave coupling in linear arrays of antiguides," *Electron. Lett.*, vol. 24, no. 21, pp. 1328–1330, 1988.

[4] D. Botez, L. J. Mawst, G. Peterson, and T. J. Roth, "Resonant optical transmission and coupling in phase-locked diode laser arrays of antiguides: The resonant optical waveguide array," *Appl. Phys. Lett.*, vol. 54, no. 22, pp. 2183–2185, 1989.

[5] J. D. Kirch *et al.*, "5.5 W near-diffraction-limited power from resonant leaky-wave coupled phase-locked arrays of quantum cascade lasers," *Appl. Phys. Lett.*, vol. 106, no. 6, 2015, Art. no. 061113.

[6] C. Sigler, C.-C. Chang, J. D. Kirch, L. J. Mawst, D. Botez, and T. Earles, "Design of resonant leaky-wave coupled phase-locked arrays of Mid-IR quantum cascade lasers," *IEEE J. Sel. Topics Quantum Electron.*, vol. 21, no. 6, Nov./Dec. 2015, Art. no. 1200810.

[7] C. Sigler *et al.*, "4.7 μm-emitting near-resonant leaky-wave-coupled quantum cascade laser phase-locked arrays," *IEEE J. Sel. Topics Quantum Electron.*, vol. 23, no. 6, Nov./Dec. 2017, Art. no. 1200706.

[8] C. Sigler *et al.*, "Spectrally resolved modal characteristics of leaky-wave-coupled quantum cascade phase-locked laser arrays," *Opt. Eng.*, vol. 57, no. 1, 2018, Art. no. 011013.

[9] W. Zhou, S. Slivken, and M. Razeghi, "Phase-locked, high power, mid-infrared quantum cascade laser arrays," *Appl. Phys. Lett.*, vol. 112, no. 18, 2018, Art. no. 181106.

[10] J. N. Walpole, "Semiconductor amplifiers and lasers with tapered gain regions," *Opt. Quantum Electron.*, vol. 28, no. 6, pp. 623–645, 1996.

[11] P. Rauter and F. Capasso, "Multi-wavelength quantum cascade laser arrays," *Laser Photon. Rev.*, vol. 9, no. 5, pp. 452–477, 2015.

[12] P. Rauter *et al.*, "Master-oscillator power-amplifier quantum cascade laser array," *Appl. Phys. Lett.*, vol. 101, no. 26, 2012, Art. no. 261117.

[13] S. Menzel *et al.*, "Quantum cascade laser master-oscillator power-amplifier with 1.5 W output power at 300 K," *Opt. Exp.,* vol. 19, no. 17, pp. 16229–16235, 2011.

[14] A. Lyakh, R. Maulini, A. Tsekoun, R. Go, and C. Kumar, and N. Patel, "Tapered 4.7 μm quantum cascade lasers with highly strained active region composition delivering over 4.5 watts of continuous wave optical power," *Opt. Exp.*, vol. 20, no. 4, pp. 4382–4388, 2012.

[15] R. Blanchard *et al.*, "High-power low-divergence tapered quantum cascade lasers with plasmonic collimators," *Appl. Phys. Lett.*, vol. 102, no. 19, 2013, Art. no. 191114.

[16] Q. Zhang *et al.*, "Thermal induced facet destructive feature of quantum cascade lasers," *Appl. Phys. Lett.*, vol. 96, no. 14, 2010, Art. no. 141117.

[17] D. Botez *et al.*, "High-efficiency, high-power mid-infrared quantum cascade lasers," *Opt. Mater. Exp.*, vol. 8, no. 5, pp. 1378–1398, 2018.

[18] A. Milton and W. Burns, "Mode coupling in optical waveguide horns," *IEEE J. Quantum Electron.*, vol. JQE-13, no. 10, pp. 828–835, Oct. 1977.

[19] J. Ryu *et al.*, "Beam stability of buried-heterostructure quantum cascade lasers employing HVPE regrowth," *Opt. Exp.*, vol. 29, no. 2, pp. 2819–2826, 2021.

[20] *Lasers and Laser-Related Equipment – Test Methods for Laser Beam Widths, Divergence Angles and Beam Propagation Ratios – Part 1: Stigmatic and Simple Astigmatic Beams*, ISO 11146-1:2005, 2005.

[21] S. Suri, B. Knipfer, J. D. Kirch, L. J. Mawst, T. Grange, and D. Botez, "Rigorous modeling of mid-IR QCLs with strong photon-induced carrier transport," in *Proc. SPIE PC12021, Novel -Plane Semicond. Lasers XXI*, 2022, Paper PC120210G. [Online]. Available: https://doi.org/10.1117/12.2610016